

ARTICLE OPEN

Magnetism and fermiology of kagome magnet $\text{YMn}_6\text{Sn}_4\text{Ge}_2$ Hari Bhandari^{1,2,3}, Rebecca L. Dally⁴, Peter E. Siegfried¹, Resham B. Regmi^{2,3}, Kirrily C. Rule^{5,6}, Songxue Chi⁷, Jeffrey W. Lynn⁴, I. I. Mazin^{1,8} and Nirmal J. Ghimire^{1,2,3}

Kagome lattice magnets are an interesting class of materials as they can host topological properties in their magnetic and electronic structures. YMn_6Sn_6 is one such compound in which various exotic magnetic and electronic topological properties have been realized. Here, by means of a partial substitution of Sn with an isovalent and slightly smaller atom Ge, we demonstrate the sensitivity of such chemical substitution on the magnetic structure and its influence in the electronic properties. Magnetic structure of $\text{YMn}_6\text{Sn}_4\text{Ge}_2$ determined by neutron diffraction reveals an incommensurate staggered magnetic spiral with a slightly larger spiral pitch than in YMn_6Sn_6 . This change in magnetic structure influences the Fermi surface enhancing the out-of-plane conductivity. Such a sensitivity to the partial chemical substitution provides a great potential for engineering the magnetic phases and associated electronic properties not only in YMn_6Sn_6 , but also in the large family of 166 rare-earth kagome magnet.

npj Quantum Materials (2024)9:6; <https://doi.org/10.1038/s41535-023-00616-0>

INTRODUCTION

Materials exhibiting exotic magnetic textures in the presence of nontrivial electronic structures have shaped the direction of much research in recent years. Investigations into these materials have led to many predictions and experimental observations of quantum phenomena including the quantum anomalous Hall effect^{1,2}, chiral Majorana modes^{3,4}, and the topological magneto-electric effect^{5,6}. These phenomena rely on the nature of the electronic structure in the presence of time-reversal symmetry breaking driven by the material's magnetism^{7–9}. An increasingly popular class of materials to investigate the interplay of topological magnetic and electronic structures are the kagome-net magnets^{10–15}.

RT_6Sn_6 compounds, where R represents a rare-earth element, and T is a 3d transition metal element, are the recent addition to the class of kagome magnets^{16–22}. In these compounds, the T atoms are arranged in the kagome geometry, and the crystal structure provides a rich materials space to tune both the electronic and magnetic properties. Compounds with non-magnetic R atoms are simpler as magnetism comes only from the T sublattice. The most widely studied, and arguably the most interesting member of this family, is YMn_6Sn_6 where multiple exotic properties have been realized including a series of competing magnetic phases and the topological Hall effect^{16,23,24}, Dirac bands^{25,26}, a rarely observed magnetization-driven Lifshitz transition²⁷, a large anomalous transverse thermoelectric effect²⁸, and an emergent electromagnetic induction²⁹.

The magnetic structure drives most of these phenomena in YMn_6Sn_6 and the interesting magnetism in this compound comes from a parametric frustration facilitated by its crystal structure shown in Fig. 1a¹⁶. It consists of Mn kagome layers in the ab -plane that are separated alternately by two distinct blocks along the c -axis: a layer containing only Sn atoms (Sn-layer) and a layer containing both Y and Sn atoms (Y-Sn layer) as depicted in Fig. 1a.

In the first approximation, the energy of this system can be described by the Hamiltonian¹⁶:

$$\mathcal{H} = \sum_{ij} J_n \mathbf{n}_i \cdot \mathbf{n}_j + \sum_{ij} J_p \mathbf{n}_i \cdot \mathbf{n}_j + \sum_i \mathcal{J} n_i^z \cdot n_{i+1}^z + K \sum_i (n_i^z)^2 + \sum_i \mathbf{n}_i \cdot \mathbf{H}, \quad (1)$$

where \mathbf{H} is the external field and \mathbf{n} is a unit vector along the local magnetization direction. The first sum runs over the three nearest neighbors along the c -axis, the second over the first nearest neighbors in the ab -plane, the next over all vertical bonds ($i+1$ denotes the nearest c -neighbor), and last two over each Mn ion. K is the single-ion anisotropy, and the Ising-type anisotropic exchange, \mathcal{J} , is the only one allowed by symmetry for the vertical bonds. As a further simplification, in our previous paper¹⁶ we limited the latter term to nearly-ferromagnetic vertical bonds only.

The in-plane interaction among the Mn atoms within a kagome layer is strongly ferromagnetic ($J_p < 0$). The spins are forced to lie in the ab -plane^{16,30} due to the net effect of the single-ion term (easy-axis) and the Ising exchange (easy-plane and stronger). The most interesting part of the magnetic order is the helical magnetic spiral at $T = 0$ and $H = 0$ which comes from the competition between J_1 , J_2 , and J_3 , and is therefore very sensitive to the stacking pattern of the Mn-layers along the c -axis. In YMn_6Sn_6 , the exchange interactions through two inequivalent layers along the c -axis within a unit cell are opposite in sign. Specifically [Fig. 1a], the interaction across the Sn-layer is ferromagnetic (FM) ($J_1 < 0$) and that across the Sn-Y layer is antiferromagnetic ($J_2 > 0$). The exchange interaction between the like-Mn layers (i.e., the next-nearest neighbor interaction) in YMn_6Sn_6 is weak and ferromagnetic $J_3 < 0$. In the absence of J_3 , a commensurate antiferromagnetic structure is expected²³. In fact, this is the case just below the Néel temperature (T_N) of 345 K. The presence of J_3 introduces parametric frustration and the system transitions into a unique

¹Department of Physics and Astronomy, George Mason University, Fairfax, VA 22030, USA. ²Department of Physics and Astronomy, University of Notre Dame, Notre Dame, IN 46556, USA. ³Stravopoulos Center for Complex Quantum Matter, University of Notre Dame, Notre Dame, IN 46556, USA. ⁴NIST Center for Neutron Research, National Institute of Standards and Technology, Gaithersburg, MD 20899, USA. ⁵Institute for Superconducting and Electronic Materials, The University of Wollongong, Wollongong, Australia. ⁶Australian Nuclear Science and Technology Organisation, New Illawarra Road, Lucas Heights, NSW 2234, Australia. ⁷Neutron Scattering Division, Oak Ridge National Laboratory, Oak Ridge, TN 37831, USA. ⁸Quantum Science and Engineering Center, George Mason University, Fairfax, VA 22030, USA. ✉email: hbhandar@gmu.edu; nghimire@nd.edu

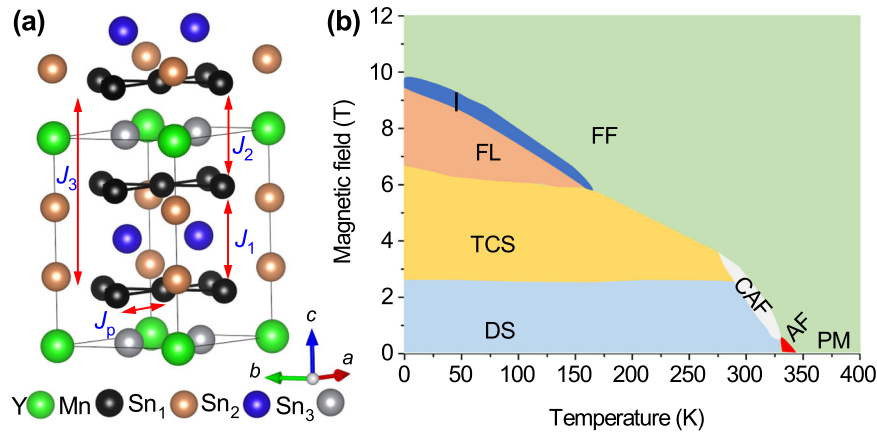


Fig. 1 Crystal structure and magnetic phase diagram of YMn_6Sn_6 . **a** Sketch of crystal structure of YMn_6Sn_6 where J_i represents the magnetic exchange interaction in different Mn planes indicated by the red lines. **b** Sketch of magnetic phase diagram of YMn_6Sn_6 stabilized by in-plane magnetic field.

Atom	Position	x	y	z
Y	1a	0	0	0
Mn	6i	1/2	0	0.24587
Sn ₁	2e	0	0	0.33679
Sn ₂	2d	1/3	2/3	1/2
Sn ₃	2c	1/3	2/3	0

The lattice parameters obtained at room temperature are: $a = b = 5.5398 \text{ \AA}$ and $c = 9.0203 \text{ \AA}$ ¹⁶.

staggered spiral phase below 333 K that persists down to the lowest measured temperatures¹⁶.

The application of an external magnetic field in the ab -plane stabilizes a series of competing magnetic phases. A sketch of the magnetic field (B)-temperature (T) phase diagram of YMn_6Sn_6 obtained in previous studies^{16,23} is depicted in Fig. 1b. At low temperatures there are four main magnetic phases, namely distorted spiral (DS), transverse conical spiral (TCS), fan-like (FL), and forced ferromagnetic (FF). In addition, there are three smaller phases labelled "I", which has a mixture of commensurate and incommensurate peaks, the canted antiferromagnetic phase (CAF), and the antiferromagnetic phase (AF)²³.

As these various magnetic structures in YMn_6Sn_6 are directly related to the crystal structure, mainly set by the spacing blocks between the Mn layers, replacement of Sn atoms by isoelectronic Ge provides a clean way to influence the magnetic properties by tuning these exchange interactions. In this work, we report the synthesis of $YMn_6Sn_4Ge_2$ and the study of its magnetic and magnetotransport properties by means of magnetic and transport measurements, and neutron diffraction experiments; and, by means of first principles calculations, we provide the microscopic insight into the influence of the magnetic structure on its electronic structure and thus the transport properties. We find that in $YMn_6Sn_4Ge_2$, Ge replaces Sn preferentially from one of the three sites [see structural details in "Crystal chemistry" and Table 1]. Directly related to this particular replacement, $YMn_6Sn_4Ge_2$ orders directly into the incommensurate spiral phase below T_N of 345 K with the spins lying in the ab -plane, and gives rise to a distinct magnetic and electronic structure. Magnetization and magnetotransport measurements show marked differences from that of the parent compound and indicate that new magnetic phases are stabilized. Counterintuitively, conductivity is enhanced, more significantly along the c -axis due to the change in

fermiology introduced by the Ge doping. Our results provide an important insight into the doping study of not only YMn_6Sn_6 , but all RMn_6Sn_6 compounds that are currently attracting significant attention for electronic and magnetic topological states.

RESULTS

Crystal chemistry

YMn_6Sn_6 crystallizes in the $HfFe_6Sn_6$ -type structure in the hexagonal space group $P6/mmm$ (#191). The crystallographic data taken from Ref.¹⁶ are presented in Table 1. In this structure, there are three inequivalent Sn positions where Sn₁, Sn₂, and Sn₃ take Wyckoff positions 2e, 2d, and 2c, respectively. Previous doping studies have reported the dopant atoms entering into different Sn positions. For example, in $YMn_6Sn_{6-x}Ga_x$, Ga enters into the 2c site³¹, while in $YMn_6Sn_{6-x}In_x$, In takes the 2d site³². An analysis of calculated x-ray diffraction patterns of $YMn_6Sn_4Ge_2$ with Ge in each of the three positions, as depicted in Fig. 2a, shows that the intensity distribution in each of these cases is distinct, which makes it easier to identify the position taken by Ge in our sample. In Fig. 2a, we plot the experimental powder x-ray diffraction pattern of $YMn_6Sn_4Ge_2$ together with the calculated patterns in different possible structures. The intensity distribution of the Bragg peaks marked by asterisks clearly shows that Ge in this compound takes the 2c position. This analysis is further verified by the Rietveld refinement of the powder x-ray pattern as shown in Fig. 2b. The results of the refinement are presented in Table 2. The best refinement result was obtained for 93% of Ge and 7% of Sn at the 2c site. For simplicity, we use the formula $YMn_6Sn_4Ge_2$ throughout this article and the same is used in the analysis of magnetic measurements as it does not make a noticeable difference. The refinement shows that the $YMn_6Sn_4Ge_2$ lattice parameters a and c are smaller than in the parent compound, with the c (a) axis shrinking by 3.8% (2.5%). It is to be noted that it is the Sn in the Sn-Y layer that is replaced by Ge in $YMn_6Sn_4Ge_2$. This essentially influences J_2 and J_3 , but leaves J_1 unaffected [see Fig. 1a].

This result is in agreement with our DFT calculations. In the latter, we first fully optimized the crystal structure with one Sn replaced by Ge in each of the three crystallographically inequivalent Sn sites. We found a very strong preference for the 2c position and the calculated total energy per formula was 0.35 eV (0.48 eV) lower than for the 2d (2e) position (see Supplementary Table 1). Next, we have fully optimized the structure of $YMn_6Sn_4Ge_2$ with Ge in the 2c position. The results are shown in Table 2 together with our experimentally obtained structure.

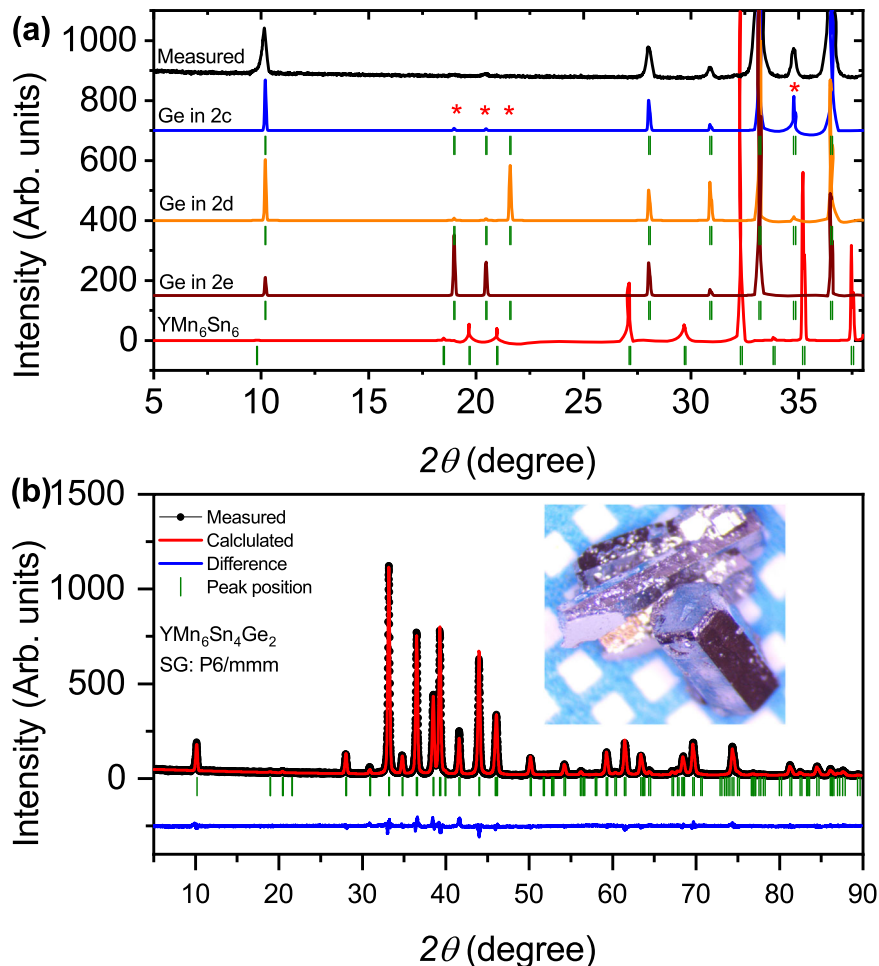


Fig. 2 Structural characterization of $\text{YMn}_6\text{Sn}_4\text{Ge}_2$. **a** Calculated powder x-ray diffraction patterns of YMn_6Sn_6 and $\text{YMn}_6\text{Sn}_4\text{Ge}_2$ with Ge in the three crystallographic sites 2c, 2d and 2e plotted together with the measured room temperature x-ray powder pattern of $\text{YMn}_6\text{Sn}_4\text{Ge}_2$. The same lattice parameters were used in the calculation for the three structures of $\text{YMn}_6\text{Sn}_4\text{Ge}_2$. Here, the x-ray powder patterns are shown between $5^\circ \leq 2\theta \leq 37^\circ$. Asterisks are used to emphasize some diffraction peaks. **b** Rietveld refinement of room temperature powder x-ray diffraction pattern of $\text{YMn}_6\text{Sn}_4\text{Ge}_2$. The model with Ge in the 2c position is used for the refinement. Inset shows an optical image of $\text{YMn}_6\text{Sn}_4\text{Ge}_2$ single crystals on a 2 mm \times 2 mm grid (blue lines on the background). The cylindrical morphology of $\text{YMn}_6\text{Sn}_4\text{Ge}_2$ single crystals is markedly different than that of the parent compound which grow in a plate-like shape. The crystallographic *c*-axis in these crystals is along the length of the cylinder.

Magnetic properties

DC magnetic susceptibility (M/B , where M is the magnetic moment and B is the external magnetic field) of $\text{YMn}_6\text{Sn}_4\text{Ge}_2$ for $B = 0.1$ T, as a function of temperature (T) is depicted in Fig. 3a. The black (red) curve is the susceptibility measured with B parallel to the *ab*-plane (*c*-axis). Both of these curves peak at 345 K indicating that the magnetic ordering takes place below this temperature.

Magnetization (M vs B) data of $\text{YMn}_6\text{Sn}_4\text{Ge}_2$ for $B \parallel c$ -axis at some representative temperatures are presented in Fig. 3b. At 1.8 K, M increases gradually with increasing B , and saturates above 8 T, attaining the saturated moment of $12.2 \mu_B$ per formula unit. This behavior of M remains the same in the entire temperature range below T_N with the exception that the saturation field and the saturated moment (as expected) decrease with increasing temperature. Above T_N (at 360 K), the M vs B curve shows a rather monotonic increase, which indicates the presence of spin correlations above T_N , expected in this class of materials, as described in Ref. 16.

Magnetization data measured with the magnetic field in the *ab*-plane are more interesting and are depicted in Fig. 3c. At 1.8 K, M first increases linearly with increasing B up to 2.2 T, where it shows a sharp jump representing a metamagnetic transition. It then

increases with increasing B , but makes a cusp-like feature, followed by a linear increase before saturating above 6 T. The saturated moment at 1.8 K is $12.8 \mu_B$ per formula unit. With increase in temperature, the metamagnetic transition remains in the entire temperature range below T_N . This transition, however, occurs at lower B as the temperature increases. The magnetic saturation field also decreases with increasing temperatures. The cusp-like feature, observed distinctly just above the metamagnetic transition at 1.8 K, gradually flattens above 100 K and is linear above 200 K.

Magnetization along the *c*-axis in $\text{YMn}_6\text{Sn}_4\text{Ge}_2$ has similar behavior as that in the parent compound, except that the saturation is attained at much smaller field (8 T vs 13 T at 1.8 K). However, the magnetization of $\text{YMn}_6\text{Sn}_4\text{Ge}_2$ in the *ab*-plane has marked differences [see Fig. 3c, d]. One similarity is that the metamagnetic transition at 1.8 K occurs at the same magnetic field of 2.2 T, but the behavior after the metamagnetic transition is quite different. While there is a cusp-like feature immediately after the metamagnetic transition in $\text{YMn}_6\text{Sn}_4\text{Ge}_2$, the parent compound has a linear M dependence and is in the TCS magnetic phase. The cusp-like feature in the parent compound appears only in the FL phase between 6.7 T and 9.8 T (at 1.8 K). The FL phase in YMn_6Sn_6 is short lived and disappears above 170 K.

Table 2. Selected data from Rietveld refinement of powder x-ray diffraction collected on ground crystals of $\text{YMn}_6\text{Sn}_4\text{Ge}_2$, and from our DFT optimization.

Space group		$P6/mmm$						
		exp.		calc.				
Unit cell a, c (Å)		5.3993(7), 8.6797(13)		5.339, 8.691				
R_{WP}		12.0%						
R_B		5.74%						
R_F		6.12%						
		exp.			calc.			
Atom	Position	x	y	z	Occupancy	x	y	z
Y	1a	0	0	0	1.00	0	0	0
Mn	6i	1/2	0	0.23245	1.00	1/2	0	0.2330
Sn ₁	2e	0	0	0.33709	1.00	0	0	0.3342
Sn ₂	2d	1/3	2/3	1/2	1.00	1/3	2/3	1/2
Sn ₃	2c	1/3	2/3	0	0.07			
Ge	2c	1/3	2/3	0	0.93	1/3	2/3	0

In Fig. 3d, we show the magnetic phase diagram of $\text{YMn}_6\text{Sn}_4\text{Ge}_2$ constructed by plotting the field derivative of magnetic moment (dM/dB) as a function of magnetic field in the temperature interval from 1.8 K to 350 K. The phase below the metamagnetic transition is the distorted spiral (DS) as this phase is similar to the DS phase of the parent compound [based on the magnetic structure determined in zero external magnetic field described in “Neutron Diffraction: Magnetic structure in zero external magnetic field” section below]. The phase at magnetic saturation is the FF phase. We mark the intermediate phases as the unknown phases U1 and U2 because these phases are different from both the TCS and FL phase of the parent compound as discussed in more details in the following sections.

Magnetotransport properties

Electrical resistivity of $\text{YMn}_6\text{Sn}_4\text{Ge}_2$ measured with the electric current applied along the c -axis (ρ_c), and in the ab -plane (ρ_{ab}) is shown by solid red and blue lines, respectively, in Fig. 4a. In each direction, the resistivity decreases with decreasing temperature indicating the metallic behavior of the material in the entire temperature range from 400 to 1.8 K. Both ρ_c and ρ_{ab} show a marked kink at 345 K indicating the reduction of the spin scattering of the charge carriers with the onset of the magnetic ordering. It is consistent with the T_N determined from susceptibility measurements in Fig. 3a. Resistivity

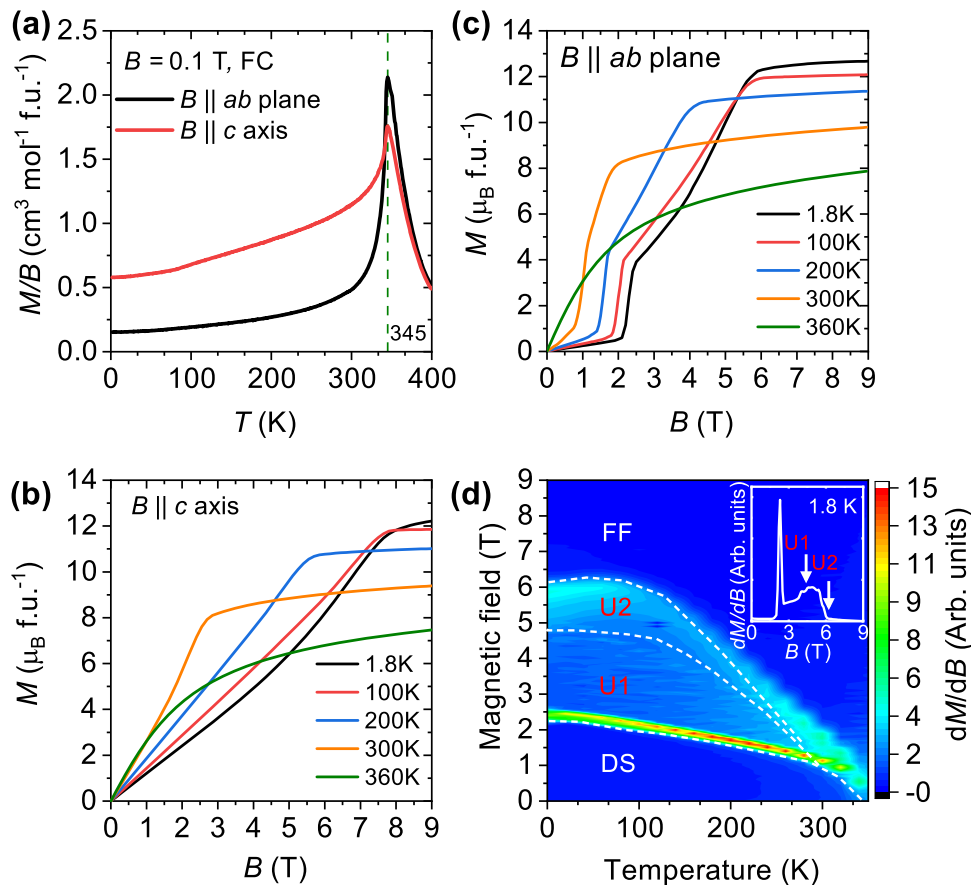


Fig. 3 **Magnetic properties of $\text{YMn}_6\text{Sn}_4\text{Ge}_2$.** **a** Magnetic susceptibility (M/B) of $\text{YMn}_6\text{Sn}_4\text{Ge}_2$ measured with a magnetic field $B = 0.1$ T, parallel and perpendicular to the c -axis. Field-cooled (FC) protocol was used for these measurements. **b, c** Magnetization M of $\text{YMn}_6\text{Sn}_4\text{Ge}_2$ as a function of external magnetic field (B) applied along the c -axis, and in the ab -plane at selected temperatures. **d** Magnetic phase diagram of $\text{YMn}_6\text{Sn}_4\text{Ge}_2$ for a magnetic field applied in the ab -plane, constructed from a color contour plot of dM/dB data measured between 1.8 K and 360 K every 20 K. The white dashed lines are guides to the eye at phase boundaries. DS and FF are distorted spiral and forced ferromagnetic phases, respectively. U1 and U2 are two unknown magnetic phases. Inset shows the magnetic field derivative of magnetization at 1.8 K.

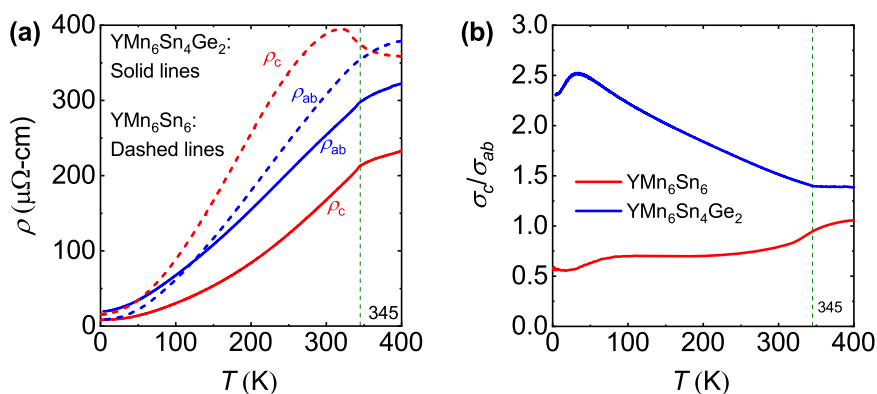


Fig. 4 Electrical resistivity and conductivity of $\text{YMn}_6\text{Sn}_4\text{Ge}_2$. **a** Electrical resistivity of $\text{YMn}_6\text{Sn}_4\text{Ge}_2$ (solid lines) and YMn_6Sn_6 (dashed lines) as a function of temperature measured with the current applied along the c -axis (ρ_c) and in the ab -plane (ρ_{ab}). The YMn_6Sn_6 data are adopted from Ref. ^{27,42}. **b** Ratio of the c -axis to ab -plane conductivity of the two compounds.

for YMn_6Sn_6 is shown for comparison by the dashed lines in Fig. 4a and is very sensitive to the spiral ordering, especially when measured with the current along the c -axis²⁷. The resistivity does not show any noticeable change when YMn_6Sn_6 orders into the commensurate antiferromagnetic phase at 345 K, but shows a remarkable change of slope at 333 K as it enters into the incommensurate spiral phase. The fact that a remarkable kink is observed in resistivity at 345 K in $\text{YMn}_6\text{Sn}_4\text{Ge}_2$ indicates that this compound directly orders into the incommensurate spiral state (which is verified by neutron diffraction, presented below). The c -axis resistivity, therefore, can provide important information about the nature of the magnetic ordering in this compound as it does in YMn_6Sn_6 . Even more interesting is that the resistivity (in either direction) in $\text{YMn}_6\text{Sn}_4\text{Ge}_2$ is smaller than that in the parent compound, more significantly along the c -axis than in the ab -plane. It suggests that the c -axis conductivity is significantly enhanced by Ge doping of YMn_6Sn_6 . This effect can be seen more clearly in Fig. 4b where the ratio of c -axis to ab -plane conductivity (σ_c/σ_{ab} , where $\sigma = 1/\rho$) for both YMn_6Sn_6 and $\text{YMn}_6\text{Sn}_4\text{Ge}_2$ are plotted between 1.8 K and 400 K. It can be seen that Ge doping, despite being isoelectronic doping, introduces a significant change in the fermiology.

To understand the effect of the different magnetic phases on magnetotransport, we measured magnetoresistance (MR). The MR is defined by $(\rho_B - \rho_0)/\rho_0 \times 100\%$ where $\rho_B(\rho_0)$ is resistivity in finite (zero) B . Let us first look at the c -axis MR (MR_c) which is depicted in Fig. 5a. At 1.8 K, MR_c first increases slightly until it reaches the metamagnetic transition, where it jumps sharply by $\approx 42\%$. With further increase in B it shows a plateau until about 4.5 T where it decreases sharply and then flattens above 6.2 T where magnetic saturation is attained. On increasing temperature, the same MR behavior persists up to 200 K. At and above 240 K, the MR decreases with increasing magnetic field above the metamagnetic transition. The overall behavior of MR measured with current in the ab -plane (MR_{ab}) as depicted in Fig. 5b is quite similar to that of MR_c , with the exception of the magnitude of jump at the metamagnetic transition, especially at lower temperatures. The MR_{ab} jump at 1.8 K is very small compared to that of MR_c as can be seen in Fig. 5c. Here, the four magnetic phases inferred from the magnetization [red curve in Fig. 5c; also see Fig. 3d] are clearly observed in the MR measurements in both directions.

Comparison of MR and magnetization for an in-plane magnetic field at 1.8 K of $\text{YMn}_6\text{Sn}_4\text{Ge}_2$ and YMn_6Sn_6 can be seen in Fig. 5c, d, respectively. First, let us compare MR_c [black curves in Fig. 5c, d]. In YMn_6Sn_6 , MR_c changes very little, if at all, at the metamagnetic transition and shows a sharp drop at around 4 T due to the Lifshitz transition²⁷. MR_c then sharply increases before entering into the FL phase, then decreases continuously, and flattens after attaining magnetic saturation (not shown here). MR_c of $\text{YMn}_6\text{Sn}_4\text{Ge}_2$, on the other hand, shows a significant jump at the metamagnetic

transition, plateaus until about 4.5 T, above which it decreases rapidly, and then flattens after entering into the saturated state. This MR_c behavior provides crucial information about the possible magnetic phases stabilized by the magnetic field in $\text{YMn}_6\text{Sn}_4\text{Ge}_2$. In our previous study of YMn_6Sn_6 ²⁷, we found that MR_c is sensitive to the angle of rotation of spins between two consecutive planes. For example, this angle changes negligibly at the DS to TCS phase transition at the metamagnetic transition, but the change is larger at the TCS to FL phase transition. Thus, the MR_c shows negligible change during the former transition while it increases by about 10% during the latter. Now, looking at MR_c of $\text{YMn}_6\text{Sn}_4\text{Ge}_2$, the fact that it increases by about 42% at the metamagnetic transition suggests that the inter-layer angle change between DS and U1 is much larger than that between the DS and TCS of the parent compound. The sharp drop in MR_c at 4.7 T is consistent with a second magnetic phase transition to U2 inferred from the magnetization data that shows a sudden slope change at the same field. The forced ferromagnetic (FF) phase is attained above 6.2 T.

Neutron diffraction: magnetic structure in zero external magnetic field

The zero-field magnetic structure of YMn_6Sn_6 has a temperature dependent periodicity along the c -axis with wavevector $\mathbf{k} = (0, 0, k_z)$, where k_z ranges from commensurate at 0.5 reciprocal lattice units (r.l.u.) just below the onset of T_N down to 0.26 r.l.u. (incommensurate) at 4 K. $\text{YMn}_6\text{Sn}_4\text{Ge}_2$ is also incommensurate along the c -axis, however, there is no sign of the initial commensurate phase. The total change in pitch between the onset of magnetic order and the lowest temperature measured is much smaller than that in the parent compound ranging from $k_z = 0.27$ r.l.u. at $T_N = 345$ K to 0.23 r.l.u. at 4 K. Fig. 6 shows a summary of the results from the Taipan experiment, where the temperature evolution of the magnetic wavevector [Fig. 6c] and area [Fig. 6d] were tracked via L -scans across the $(0, 0, 2) + \mathbf{k}$ Bragg peak. At lower temperatures, a one-peak Gaussian fit is sufficient to analyze the data. However, at temperatures above ≈ 100 K, the FWHM of the Bragg peak monotonically increases with increasing temperature, with values larger than that of the calculated instrumental resolution. Above ≈ 320 K, it is clear that there are actually two magnetic Bragg peaks in close proximity to one another (similar to that in the parent compound). Fits comprised of two Gaussian peaks were therefore used to analyze the temperature dependent parameters. The FWHM of each Gaussian peak was fixed to be that of the calculated instrumental resolution for the $(0, 0, 2) + \mathbf{k}$ position (0.018 \AA^{-1}). The peak with the smaller- q value is denoted by the wavevector, \mathbf{k}_1 , and the peak with the larger- q value is denoted by the wavevector, \mathbf{k}_2 . The fits for representative data at 15, 260, and 330 K can be seen in Fig. 6b. The neutron data show that the magnetic structure associated with the \mathbf{k}_2 wavevector is dominant as

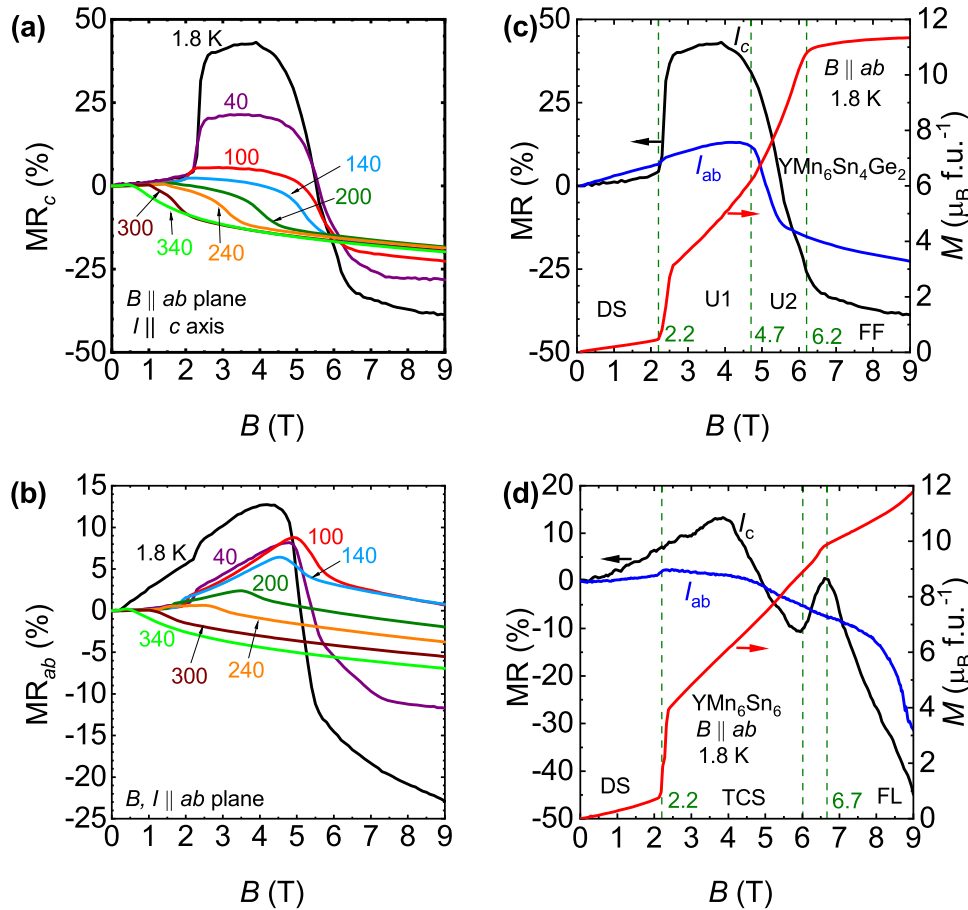


Fig. 5 Magnetoresistance and magnetization of $\text{YMn}_6\text{Sn}_4\text{Ge}_2$ and YMn_6Sn_6 . Magnetoresistance of $\text{YMn}_6\text{Sn}_4\text{Ge}_2$ at selected temperatures measured with current applied along the (a) c -axis, and (b) in the ab -plane. Magnetoresistance (black and blue lines, left axis) and Magnetization (red line, right axis) of (c) $\text{YMn}_6\text{Sn}_4\text{Ge}_2$, and (d) YMn_6Sn_6 at 1.8 K. The YMn_6Sn_6 data in (d) are adopted from Ref. ^{27,42}. In each MR measurement, the magnetic field was applied in the ab -plane. In (c, d) the black (blue) curve represents the MR measured with current applied along the c -axis, I_c (ab -plane, I_{ab}). The green dashed lines in (c, d) are a guide to eye for the indicated magnetic fields. It is to be noted that demagnetization considerations in these materials do not significantly affect the comparison between MR vs B and M vs B ²⁷.

compared to that belonging to \mathbf{k}_1 , although it does appear that the \mathbf{k}_1 magnetic Bragg peak persists to the base temperature measured [fit results for the \mathbf{k}_1 structure are shown in Supplementary Fig. 1c, d]. This contrasts with the parent compound, where the volume of the \mathbf{k}_1 and \mathbf{k}_2 magnetic domains is approximately equal throughout the same temperature range.

The power law, $I = I_0(1 - \frac{T}{T_N})^{2\beta}$, was fit to the integrated area data for the Bragg peak, $(0, 0, 2) + \mathbf{k}_2$, shown as the solid line in Fig. 6d. The fit was performed using only data points near T_N , between 300 and 346 K, with $I_0 = 14.0 \pm 0.6$, $T_N = 345.95 \text{ K} \pm 0.02 \text{ K}$, and $\beta = 0.323 \pm 0.008$. The β value extracted from the power law fit is $\approx \frac{1}{3}$, which is typical for various three-dimensional magnetic materials.

Data from the HB-3 triple-axis spectrometer were used to refine the nuclear [Supplementary Fig. 1a] and magnetic structure. Data were collected as $\theta - 2\theta$ scans across Bragg peaks, and the integrated area of Gaussian fits to the peaks were corrected for the Lorentz factor to extract the observed structure factor, $|F_{obs}^2|$. These values were used to refine the magnetic structure using the program, FULLPROF³³, and the results are shown in Fig. 7. Irreducible representational analysis was used to model the structure and the details of the refinement can be found in the Supplementary Note 1. The refined structure is the staggered spiral where all moments within a Mn kagome plane are ferromagnetically ordered and constrained to the ab -plane. The moments between Mn planes (along the c -axis) are rotated relative to one another by an angle α within a unit cell (between

Mn layers separated by the Sn-layer) and by an angle β between unit cells (i.e., between the Mn layers separated by the Sn-Y layer) [see Fig. 1a]. The sum $\alpha + \beta$ determines the pitch length, and hence wavevector, of the spiral. At 1.5 K, $\mathbf{k} = (0, 0, 0.23)$ and the refined value $\alpha = 7.9(7)^\circ$, leading to a value of $\beta = 75.0(7)^\circ$. The total ordered moment per Mn atom is $2.19(3) \mu_B$. A smaller set of data was collected at 250 K, where the refinement yielded $\mu = 1.61(8) \mu_B$ and $\alpha = 4(2)^\circ$, with an agreement $R_F = 10.6$ [refinement shown in Supplementary Fig. 1b]. The refined moment values at both 1.5 K and 250 K are in agreement with those from magnetization measurements [Fig. 3b, c].

DISCUSSION

One marked difference between $\text{YMn}_6\text{Sn}_4\text{Ge}_2$ and YMn_6Sn_6 observed in neutron diffraction data at base temperature is in the spiral pitch, k_z , which is 0.23 ($T = 1.5 \text{ K}$) in the former compound and 0.26 ($T = 4 \text{ K}$) in the latter. As such, the refined values of the two turning angles, α and β , in $\text{YMn}_6\text{Sn}_4\text{Ge}_2$ are 7.9° and 75.0° . These angles are quite different in the parent compound where $\alpha \approx -5^\circ$, and $\beta \approx 99^\circ$ (the Supplementary Table 3 contains a quick reference to these comparisons). This suggests that unlike the parent compound where $J_1 < 0$ and $J_2 > 0$, both of these exchange interactions are negative (i.e. $J_{1,2} < 0$) in $\text{YMn}_6\text{Sn}_4\text{Ge}_2$. In fact, the ratio of the exchange interactions J_2/J_1 and J_3/J_1 can be calculated from α and β using the following

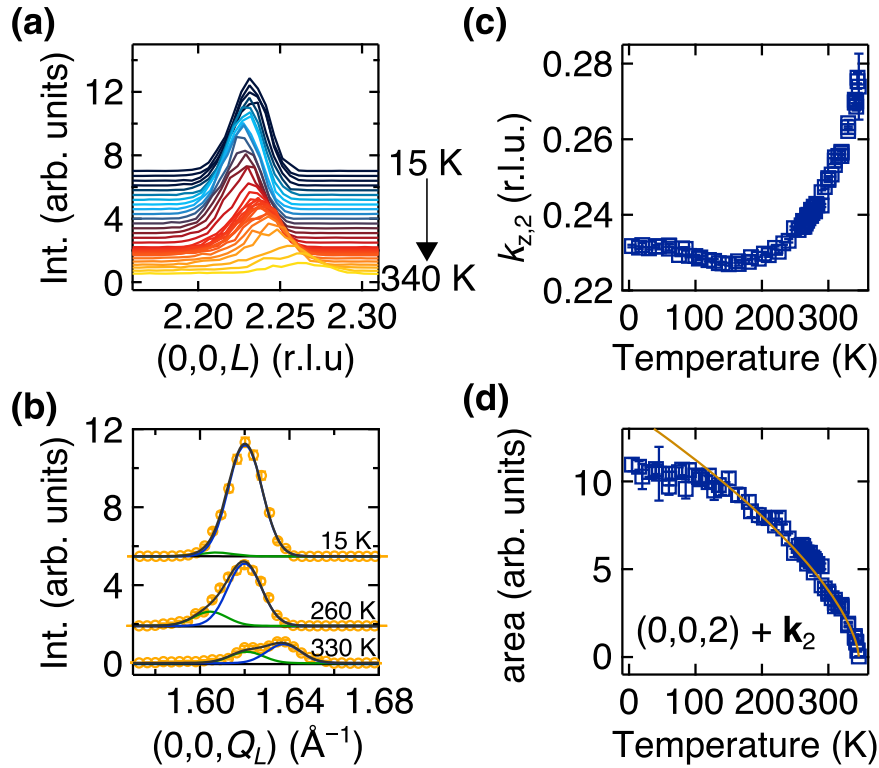


Fig. 6 Neutron diffraction of $\text{YMn}_6\text{Sn}_4\text{Ge}_2$. *L*-scans spanning the magnetic Bragg peaks at $(0, 0, 2) + \mathbf{k}_2$. **a** Scans between 15 K and 340 K, where scans are offset from one another along the intensity-axis by an amount proportional to the temperature. **b** Individual scans at 15 K, 260 K, and 330 K, offset along the intensity-axis for clarity, with two-Gaussian fits to the data. The green solid line is the fit for the \mathbf{k}_1 magnetic peak, and the blue solid line is the fit for \mathbf{k}_2 . The black and grey solid lines are for the linear background and the total fit, respectively. **c** The evolution of the \mathbf{k}_2 wavevector and **(d)** the area of the $(0, 0, 2) + \mathbf{k}_2$ magnetic peak with temperature. The solid orange line in **(d)** is a power law fit to the data.

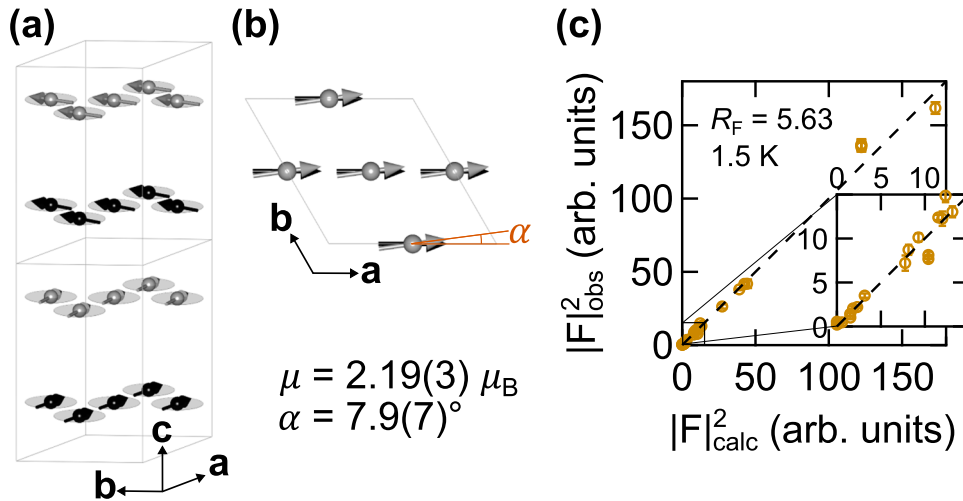


Fig. 7 Magnetic structure of $\text{YMn}_6\text{Sn}_4\text{Ge}_2$ at 1.5 K. **a** View of the magnetic structure showing the moment rotation along the *c*-axis. Only Mn atoms are shown and the two layers of Mn atoms within a unit cell are shaded black and grey. The nuclear unit cell boundaries are outlined in grey. **b** View of the magnetic structure in the *ab*-plane of one unit cell. The Mn atoms within a unit cell are nearly ferromagnetically aligned, however, a small angle $\alpha = 7.9(7)^\circ$ separates them. **c** The results of the magnetic structure refinement at 1.5 K, where the agreement between the observed ($|F|_{\text{obs}}^2$) and calculated ($|F|_{\text{calc}}^2$) structure factor is $R_F = 5.63$.

relations^{16,34}:

$$\alpha = -\text{sign}(J_1 J_3) \cos^{-1} \left(\frac{J_2 J_3}{J_1^2} - \frac{J_3}{J_2} - \frac{J_2}{4J_3} \right), \quad (2)$$

$$\beta = \cos^{-1} \left(\frac{J_3 J_1}{J_2^2} - \frac{J_1}{4J_3} - \frac{J_3}{J_1} \right), \quad (3)$$

$$\alpha + \beta = \cos^{-1} \left(\frac{J_1 J_2}{8J_3^2} - \frac{J_2}{2J_1} - \frac{J_1}{2J_2} \right). \quad (4)$$

Experimental values of α , and β yield $J_2/J_1 = 0.142$ and $J_3/J_1 = -0.0692$, confirming that J_1 and J_2 are both ferromagnetic in $\text{YMn}_6\text{Sn}_4\text{Ge}_2$. This means that replacing Sn by Ge in the 2c position reverses the sign of both J_2 and J_3 . As one can anticipate, the effect of Ge substitution is the strongest regarding J_2 , but the effect on J_3 , while sign-changing, is small in terms of the absolute change. The change of sign of J_2 is a large and unexpected effect. Indeed, intercalating a magnetic ion such as Tb, in the same plane, leads to an effective ferromagnetic J_1 interaction, which is readily understood in terms of exchange coupling between Tb and Mn^{20,35} (regardless of the sign of the Tb-Mn exchange coupling). Ge is nonmagnetic, so the sign change, on the first glance, seems rather mysterious.

A useful hint is provided by our resistivity measurements, which show that Ge substitution increases the conductivity along the z direction (where $z \parallel c$ -axis here) [Fig. 4a], thus making the material more metallic. This is consistent with the DFT calculations, which show the Fermi surface with quasi-2D sheets (in the spin-majority channel), which is absent in the parent compound [Fig. 8a, b]^{16,27}. Direct calculations of the plasma frequency squared (ω_p^2), which

determines the conductivity in the single scattering rate approximation, also support this assertion; the calculated (ω_p^2)_z increases by 50% upon Ge substitution as shown in Fig. 8c (the in-plane conductivity also increases, albeit less, but is irrelevant for this discussion)!. The calculated σ_c/σ_{ab} presented in Fig. 8c agrees well with the experimental data depicted in Fig. 4b. Furthermore, better metallicity translates into a kinetic energy advantage for a ferromagnetic coupling, which is exactly what we deduced from our neutron measurements.

This provides insight into the role of Ge substitution at the 2c position for both the magnetic ordering and fermiology of $\text{YMn}_6\text{Sn}_4\text{Ge}_2$ that change both the magnetic and transport properties measured in zero or small magnetic fields. These changes in magnetic and electronic structures are certainly responsible for the observed marked difference in the magnetic phases and the magnetoresistance behavior at higher magnetic field. Magnetic field dependent neutron diffraction experiments are required to determine the magnetic structure stabilized at the higher magnetic fields. More importantly, it will also be intriguing to perform several other measurements such as ARPES, STM²⁶, thermoelectric effect²⁸, and electromagnetic induction²⁹ to understand the role of the altered magnetic and electronic structure in these various properties observed in the parent compound YMn_6Sn_6 .

$\text{YMn}_6\text{Sn}_4\text{Ge}_2$ is a compound between YMn_6Sn_6 and YMn_6Ge_6 . Both of the end compounds first order into the commensurate antiferromagnetic structure, with YMn_6Sn_6 (YMn_6Ge_6) having easy plane (easy axis) anisotropy in the entire temperature range. In contrast to both of the end compounds, $\text{YMn}_6\text{Sn}_4\text{Ge}_2$ orders directly into an incommensurate spiral state. In addition, and interestingly, the saturation magnetic field of $\text{YMn}_6\text{Sn}_4\text{Ge}_2$ (6 T) is

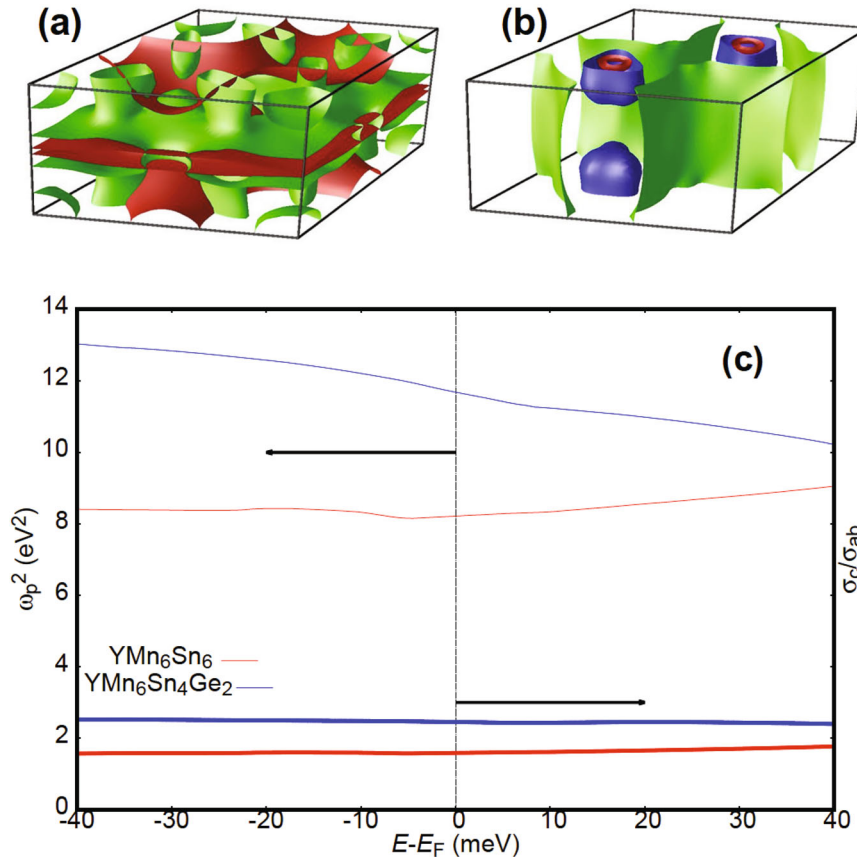


Fig. 8 Calculated electronic and transport properties of $\text{YMn}_6\text{Sn}_4\text{Ge}_2$ and YMn_6Sn_6 . Calculated Fermi surface of ferromagnetic $\text{YMn}_6\text{Sn}_4\text{Ge}_2$ for (a) spin majority, and (b) spin minority bands (c) Calculated c -axis plasma frequency squared (ω_p^2)_z (left axis), and ratio of c -axis to ab -plane conductivity (right axis), for the Fermi surface depicted in (a, b) (blue lines), and those of YMn_6Sn_6 (red lines).

smaller than that of both YMn_6Sn_6 (9.8 T) and YMn_6Ge_6 (>30 T), despite the fact that complete replacement of Sn by Ge leads to a threefold increase of the saturation field. This is an indication that partial replacement of Ge in the RMn_6Sn_6 compounds leads to markedly different magnetic and transport properties than one would expect from just a linear interpolation between the two compounds. Our study thus provides a new prospective into the study of the R166 stannates to tune the magnetic and magnetotransport properties.

In summary, we have performed systematic transport, magnetic, and neutron diffraction experiments in a wide temperature and magnetic field range on single crystals of $\text{YMn}_6\text{Sn}_4\text{Ge}_2$. The experimental studies have been supported by DFT calculations. Our magnetotransport measurements confirm that the magnetic structure of the parent compound YMn_6Sn_6 can be tuned through Ge doping. From neutron diffraction, we observed that this compound orders directly into an incommensurate staggered spiral magnetic structure that persists from the Néel temperature to 1.5 K. An in-plane external magnetic field stabilizes two magnetic phases that are markedly different from those in the parent compound. Both experimental and calculated results reveal that Ge substitution onto the 2c site alters the signs of the interplanar exchange interactions J_2 and J_3 influencing the pitch of the staggered spiral. This change in magnetic structure influences the Fermi surface making the material more conductive along the *c*-axis. Altogether, our detailed studies of the kagome magnet, $\text{YMn}_6\text{Sn}_4\text{Ge}_2$, provide important information that will be crucial in understanding the magnetotransport properties and the magnetic structures in the class of R166 kagome magnets that is currently attracting a great deal of interest for both magnetic and electronic topological states.

METHODS

Crystal growth

Single crystals of $\text{YMn}_6\text{Sn}_4\text{Ge}_2$ were grown by the self-flux method using Sn as a flux. Y pieces (Alfa Aesar; 99.9%), Mn pieces (Alfa Aesar; 99.95%), Sn shots (Alfa Aesar; 99.999%), and Ge pieces (Alfa Aesar; 99.9999%) were loaded into a 2-ml aluminum oxide crucible in a molar ratio of 1:6:18:2. The crucible was then sealed in a fused silica ampule under vacuum. The sealed ampule was heated to 1150 °C over 10 h, kept at 1150 °C for 10 h, and then cooled to 650 °C at the rate of 5 °C/h. Once the furnace reached 650 °C, the tube was centrifuged to separate the crystals in the crucible from the molten flux. Several well-faceted hexagonal crystals [see the inset in Fig. 2b for an optical image of the crystals] up to 40 mg were obtained in the crucible.

Powder x-ray diffraction

The crystal structure was verified by Rietveld refinement³⁶ of a powder x-ray diffraction pattern collected on a pulverized single crystal using a Rigaku Miniflex diffractometer with a copper target. The Rietveld refinement was performed using the FULLPROF software³³. As it was clear from the comparison of powder pattern with simulations shown in Fig. 2a that Ge has replaced Sn from 2c site, only the occupancy of Ge and Sn in 2c site was refined.

Magnetic and magnetotransport measurements

DC magnetization, resistivity, and magnetoresistance measurements were performed in a Quantum Design Dynacool Physical Property Measurement System (PPMS) with a 9 T magnet. ACMS II option was used in the same PPMS for DC magnetization measurements. Single crystals of $\text{YMn}_6\text{Sn}_4\text{Ge}_2$ were trimmed to adequate dimensions for electrical transport measurements. Crystals were oriented with the [0,0,1] and [1,1,0] directions parallel to the applied field for the *c*-axis and *ab*-plane measurements. Resistivity and Hall measurements were performed using the 4-probe method. Pt wires of 25 μm were used

for electrical contacts with contact resistances <30 Ohms. Contacts were affixed with Epotek H20E silver epoxy. An electric current of 2 mA was used for the electrical transport measurements. Contact misalignment in the magnetoresistance measurement was corrected by symmetrizing the measured data in positive and negative magnetic fields. The magnetic and magnetotransport data (with current along *c*-axis) presented here were measured on the same single crystal. First, magnetic properties were measured in both directions. Then the same crystal was polished to measure the magnetotransport measurements. The resistivity and magnetotransport data with current in the *ab*-plane were measured in a second crystal from the same growth batch after characterizing the magnetic properties.

Neutron diffraction

Neutron diffraction data were taken on the thermal triple-axis neutron spectrometer, TAIPAN³⁷, at the Australian Centre for Neutron Scattering. A PG(002) vertically focusing monochromator and a PG(002) flat analyzer were used at a wavelength of 2.345 Å. Söller slit collimators with full-width-at-half-maximum (FWHM) angular divergences of 30'-20'-20' were placed before the monochromator, before the sample, and after the sample. Data were taken between temperatures of 360 K and 4 K using a cryofurnace with He exchange gas for temperatures below 290 K. The sample used was a 19.7 mg single crystal of $\text{YMn}_6\text{Sn}_4\text{Ge}_2$ oriented in the (*H*, *H*, *L*) scattering plane. The sample mosaic was determined to be 0.37°, reflective of a good quality crystal. Additional neutron diffraction data were taken on the thermal triple-axis neutron spectrometer, HB-3, at the High Flux Isotope Reactor at Oak Ridge National Laboratory. A PG(002) vertically focusing monochromator and a PG(002) flat analyzer were used at a wavelength of 2.359 Å. Söller slit collimators with FWHM angular divergences of 48'-20'-20'-70' were placed before the monochromator, before the sample, after the sample, and after the analyzer. The sample was the same single crystal used in the TAIPAN experiment, but the crystal was oriented in the (*H*, 0, *L*) scattering plane and placed in a cryostat (1.5–300 K).

Density functional theory calculations

For the density functional theory (DFT) calculations we first used a projector augmented wave basis as implemented in the Vienna ab initio simulation package (VASP)^{38,39}, for structure optimization, and then used an augmented plane wave code WIEN2K⁴⁰ for Fermi surface analysis. In all cases a generalized gradient approximation for the exchange and correlation functional⁴¹ was utilized. No LDA+U or other corrections beyond DFT were applied. Up to $11 \times 11 \times 6$ k-point mesh (64 irreducible points) was used to structural optimization, and $48 \times 48 \times 25$ for the Fermi surface and transport analyses.

Error bars displayed in plots and uncertainties listed throughout the manuscript represent plus and minus one standard deviation.

DATA AVAILABILITY

The authors declare that the main data supporting the findings of this study are available within the article and its Supplementary Information files. Extra data are available from the corresponding author upon request.

Received: 29 March 2023; Accepted: 22 December 2023;

Published online: 08 January 2024

REFERENCES

1. Liu, C.-X., Zhang, S.-C. & Qi, X.-L. The quantum anomalous Hall effect: theory and experiment. *Annu. Rev. Condens. Mater. Phys.* **7**, 301 (2016).
2. Chang, C.-Z. et al. Experimental observation of the quantum anomalous hall effect in a magnetic topological insulator. *Science* **340**, 167 (2013).

3. Akhmerov, A., Nilsson, J. & Beenakker, C. Electrically detected interferometry of Majorana fermions in a topological insulator. *Phys. Rev. Lett.* **102**, 216404 (2009).
4. Daido, A. & Yanase, Y. Majorana flat bands, chiral Majorana edge states, and unidirectional Majorana edge states in noncentrosymmetric superconductors. *Phys. Rev. B* **95**, 134507 (2017).
5. Lee, Y.-L., Park, H. C., Ihm, J. & Son, Y.-W. Manifestation of axion electrodynamics through magnetic ordering on edges of a topological insulator. *Proc. Natl Acad. Sci.* **112**, 11514 (2015).
6. Wu, L. et al. Quantized Faraday and Kerr rotation and axion electrodynamics of a 3D topological insulator. *Science* **354**, 1124 (2016).
7. Haldane, F. D. M. Model for a quantum hall effect without landau levels: condensed-matter realization of the “parity anomaly”. *Phys. Rev. Lett.* **61**, 2015 (1988).
8. Ohgushi, K., Murakami, S. & Nagaosa, N. Spin anisotropy and quantum hall effect in the kagomé lattice: chiral spin state based on a ferromagnet. *Phys. Rev. B* **62**, R6065 (2000).
9. Armitage, N. P., Mele, E. J. & Vishwanath, A. Weyl and Dirac semimetals in three-dimensional solids. *Rev. Mod. Phys.* **90**, 015001 (2018).
10. Zhang, Z.-Y. The quantum anomalous Hall effect in kagomé lattices. *J. Phys. Condens. Mater.* **23**, 365801 (2011).
11. Ghimire, N. J. & Mazin, I. I. Topology and correlations on the kagome lattice. *Nat. Mater.* **19**, 137 (2020).
12. Kang, M. et al. Dirac fermions and flat bands in the ideal kagome metal FeSn. *Nat. Mater.* **19**, 163 (2020).
13. Ye, L. et al. Massive Dirac fermions in a ferromagnetic kagome metal. *Nature* **555**, 638 (2018).
14. Yin, J.-X. et al. Negative flat band magnetism in a spin-orbit-coupled correlated kagome magnet. *Nat. Phys.* **15**, 443 (2019).
15. Kuroda, K. et al. Evidence for magnetic weyl fermions in a correlated metal. *Nat. Mater.* **16**, 1090 (2017).
16. Ghimire, N. J. et al. Competing magnetic phases and fluctuation-driven scalar spin chirality in the kagome metal YMn_6Sn_6 . *Sci. Adv.* **6**, eabe2680 (2020).
17. Arachchige, H. W. S. et al. Charge density wave in kagome lattice intermetallic ScV_6Sn_6 . *Phys. Rev. Lett.* **129**, 216402 (2022).
18. Rosenberg, E. et al. Uniaxial ferromagnetism in the kagome metal TbV_6Sn_6 . *Phys. Rev. B* **106**, 115139 (2022).
19. Pokharel, G. et al. Electronic properties of the topological kagome metals YV_6Sn_6 and GdV_6Sn_6 . *Phys. Rev. B* **104**, 235139 (2021).
20. Jones, D. C. et al. Origin of spin reorientation and intrinsic anomalous hall effect in the kagome ferrimagnet TbMn_6Sn_6 . *arXiv* <https://arxiv.org/abs/2203.17246> (2022).
21. Ma, W. et al. Rare earth engineering in RMn_6Sn_6 ($R = \text{Gd} - \text{Tm}, \text{Lu}$) topological kagome magnets. *Phys. Rev. Lett.* **126**, 246602 (2021).
22. Pokharel, G. et al. Highly anisotropic magnetism in the vanadium-based kagome metal TbV_6Sn_6 . *Phys. Rev. Mater.* **6**, 104202 (2022).
23. Dally, R. L. et al. Chiral properties of the zero-field spiral state and field-induced magnetic phases of the itinerant kagome metal YMn_6Sn_6 . *Phys. Rev. B* **103**, 094413 (2021).
24. Wang, Q. et al. Field-induced topological hall effect and double-fan spin structure with a c-axis component in the metallic kagome antiferromagnetic compound YMn_6Sn_6 . *Phys. Rev. B* **103**, 014416 (2021).
25. Li, M. et al. Dirac cone, flat band and saddle point in kagome magnet YMn_6Sn_6 . *Nat. Commun.* **12**, 3129 (2021).
26. Li, H. et al. Manipulation of dirac band curvature and momentum-dependent g factor in a kagome magnet. *Nat. Phys.* **18**, 644 (2022).
27. Siegfried, P. E. et al. Magnetization-driven lifshitz transition and charge-spin coupling in the kagome metal YMn_6Sn_6 . *Commun. Phys.* **5**, 58 (2022).
28. Roychowdhury, S. et al. Large room temperature anomalous transverse thermoelectric effect in kagome antiferromagnet YMn_6Sn_6 . *Adv. Mater.* **34**, 2201350 (2022).
29. Kitaori, A. et al. Emergent electromagnetic induction beyond room temperature. *Proc. Natl Acad. Sci. USA* **118**, e2105422118 (2021).
30. Venturini, G., Fruchart, D. & Malaman, B. Incommensurate magnetic structures of RMn_6Sn_6 ($R = \text{Sc}, \text{Y}, \text{Lu}$) compounds from neutron diffraction study. *J. Alloy. Compd.* **236**, 102 (1996).
31. Lefèvre, C., Venturini, G. & Malaman, B. Neutron diffraction study of $\text{HfFe}_x\text{Ge}_{6-x}$ -type $\text{TmMn}_6\text{Sn}_{6-x}\text{Ga}_x$ compounds ($0.0 \leq x \leq 2.5$). *J. Alloy. Compd.* **346**, 84 (2002).
32. Lefèvre, C., Verniere, A., Venturini, G. & Malaman, B. A neutron diffraction study of $\text{HfFe}_x\text{Ge}_{6-x}$ -type $\text{YMn}_6\text{Sn}_{6-x}\text{In}_x$ compounds ($0.03 \leq x \leq 0.72$). *J. Alloy. Compd.* **361**, 40 (2003).
33. Rodríguez-Carvajal, J. Recent advances in magnetic structure determination by neutron powder diffraction. *Phys. B* **192**, 55 (1993).
34. Rosenfeld, E. V. & Mushnikov, N. V. Double-flat-spiral magnetic structures: theory and application to the RMn_6X_6 compounds. *Phys. B* **403**, 1898 (2008).
35. Lee, Y. et al. Interplay between magnetism and band topology in Kagome magnets RMn_6Sn_6 . *arXiv* <https://arxiv.org/abs/2201.11265> (2022).
36. McCusker, L. B. et al. Rietveld refinement guidelines. *J. Appl. Cryst.* **32**, 36 (1999).
37. Danilkin, S., Horton, G., Moore, R., Braoudakis, G. & Hagen, M. The TAI-PAN thermal triple-axis spectrometer at the OPAL reactor. *J. Neutr. Res.* **15**, 55 (2007).
38. Kresse, G. & Furthmüller, J. Efficiency of ab-initio total energy calculations for metals and semiconductors using a plane-wave basis set. *Comput. Mater. Sci.* **6**, 15 (1996).
39. Kresse, G. & Furthmüller, J. Efficient iterative schemes for ab initio total-energy calculations using a plane-wave basis set. *Phys. Rev. B* **54**, 11169 (1996).
40. Blaha, P. et al. Wien2k: An APW+lo program for calculating the properties of solids. *J. Chem. Phys.* **152**, 074101 (2020).
41. Perdew, J. P., Burke, K. & Wang, Y. Generalized gradient approximation for the exchange-correlation hole of a many-electron system. *Phys. Rev. B* **54**, 16533 (1996).
42. Siegfried, P. E. et al. Distributed under a creative commons attribution 4.0 international license. *Commun. Phys.* <https://doi.org/10.1038/s42005-022-00833-2> (2022).

ACKNOWLEDGEMENTS

N.J.G. and H.B. acknowledge the support from the NSF CAREER award DMR-2143903. Crystal growth part of the work at George Mason University was supported by the U.S. Department of Energy, Office of Science, Basic Energy Sciences, Materials Science and Engineering Division. I.I.M. acknowledges support from the U.S. Department of Energy through the grant No. DE-SC0021089. Research conducted at ORNL's High Flux Isotope Reactor was sponsored by the Scientific User Facilities Division, Office of Basic Energy Sciences, US Department of Energy. The authors would like to acknowledge the support from the Australian Centre for Neutron Scattering through proposal P9799. The identification of any commercial product or trade name does not imply endorsement or recommendation by the National Institute of Standards and Technology.

AUTHOR CONTRIBUTIONS

N.J.G. and H.B. conceived the idea and coordinated the project. H.B. grew single crystals. R.B.R. helped in the crystal growth. H.B. and P.E.S. performed magnetic and magnetotransport measurement. H.B. carried out the data analysis. R.L.D., J.W.L., K.C.R., and S.C. contributed to neutron diffraction experiments. R.L.D. analysed the neutron data and wrote the neutron part. I.I.M. contributed to the DFT calculations. H.B. and N.J.G. wrote the manuscript with input from I.I.M. All authors contributed to the discussion of the results.

COMPETING INTERESTS

The authors declare no competing interests.

ADDITIONAL INFORMATION

Supplementary information The online version contains supplementary material available at <https://doi.org/10.1038/s41535-023-00616-0>.

Correspondence and requests for materials should be addressed to Hari Bhandari or Nirmal J. Ghimire.

Reprints and permission information is available at <http://www.nature.com/reprints>

Publisher's note Springer Nature remains neutral with regard to jurisdictional claims in published maps and institutional affiliations.



Open Access This article is licensed under a Creative Commons Attribution 4.0 International License, which permits use, sharing, adaptation, distribution and reproduction in any medium or format, as long as you give appropriate credit to the original author(s) and the source, provide a link to the Creative Commons license, and indicate if changes were made. The images or other third party material in this article are included in the article's Creative Commons license, unless indicated otherwise in a credit line to the material. If material is not included in the article's Creative Commons license and your intended use is not permitted by statutory regulation or exceeds the permitted use, you will need to obtain permission directly from the copyright holder. To view a copy of this license, visit <http://creativecommons.org/licenses/by/4.0/>.

© The Author(s) 2024